Simulating human sleep spindle MEG and EEG from ion channel and circuit level dynamics

Rosen[1,*], B.Q., Krishnan[2,*] G.P., Sanda[2], P., Komarov[2], M., Sejnowski[1,3], T., Rulkov[4], N., Bazhenov[1,2,^] ,M., Halgren[1,2,^], E.

*co-first

^co-senior

1. Neuroscience Graduate Program, University of Californa, San Diego, La Jolla CA

2. School of Medicine, University of California, San Diego, La Jolla CA

3. The Salk Institute, La Jolla CA

4. BioCiruits Institute, University of California, San Diego, La Jolla CA

Abstract

Although they form a unitary phenomenon, the relationship between extracranial MEG/EEG and transmembrane ion flows is understood only as a general principle rather than as a well-articulated and quantified causal chain. Here we present an integrated multiscale model, beginning with a computational neural model of the thalamus and cortex during stage N2 non-REM sleep. This network model generated sleep spindles due to the interactions of local and distant network connections and intrinsic currents within thalamocortical circuits, as specified based on the previous experiments and computational works. The core spindle activity, generated by interaction of thalamic relay and reticular neurons was projected to the cortex. The 32,652 cortical neurons were mapped onto the cortical surface reconstructed from a subject's MRI, and they were interconnected based on cortical geodesic distances. MRI was used to specify a boundary element model of the subject's brain, CSF, skull and scalp. The model generated cortical activity during spindles was then projected to the MEG and EEG sensors. Dipole strength was based on multi-microelectrode laminar recordings in humans. The resulting simulated spindles were found to be similar in amplitude and topography to those actually recorded in the same subject. This similarity of the modeled and empirical spindles was subject-specific. We found that spindles modeled as originating in core thalamocortical systems were more similar to spindles recorded with MEG than EEG, and conversely, modeled matrix spindles were more similar to recorded EEG than MEG spindles. This multiscale model provides a platform for the principled quantitative integration of existing information relevant to the generation of sleep spindles, and allows the implications of future findings to be explored. It provides a proof of principle for a methodological framework allowing large-scale integrative brain oscillations to be understood in terms of their underlying channels and synapses.

Keywords

MEG, EEG, Forward Model, Sleep, Spindle, Thalamocortical

Introduction

Neuroscientific phenomena both manifest and are investigated at an incredible range of spatial scales. Magneto- and electroencephalography (M/EEG), are complementary, non-invasive, temporal-resolved, and, in the later case, inexpensive, measures of human neural activity. While the source of these signals are ultimately microscopic cellular post-synaptic currents, the relationship between the two is obscured by the complex cancellation and summation among the many thousands or millions of neurons contributing to any single sensor's leadfield (Cohen, 2017). Here we present an initial effort to traverse the spatial scales by integrating simulations of large networks of neurons with biophysical models of electromagnetic propagation, informed by non-invasive imaging and invasive recordings in humans, as well as decades of work in animal models.

While there have been prior efforts to estimate M/EEG generated by simulated whole-brain networks of neurons (Costa et al., 2016; Deco et al., 2008; Ritter et al., 2013), these models oversimplify or ignore necessary details of individual neuron behavior. Take, for example, sleep spindles: spontaneous burst or 10-16 Hz activity lasting 0.5-3 seconds which are the hallmark of stage 2 non-REM (N2) sleep, and which do not occur in isolated cortex (Andersen et al., 1967). Simulating this behavior require detailed cellular mechanics such as hyperpolarization-activated cation current,I_h (Destexhe et al., 1996; McCormick and Pape, 1990) and low-threshold Ca^{2+} current I_T (Huguenard and McCormick, 1992; Huguenard and Prince, 1992). While Costa and colleagues (Costa et al., 2016), included these details in their neural mass model, their EEG forward modeling only considered an anatomically and physiologically implausible point source.

Empirical sleep M/EEG and structural MRI were collected to provide a basis for model evaluation and donor cortical and cranial substrates in which to embed simulated neurons. In our framework, the neural activity of individual persons is modeled, as connections among neurons are derived in part from the cortical geometry of the subject against whose data the model will be compared. Microscopic cellular currents are scaled to mesoscopic equivalent dipoles using factors derived from human laminar electrode data. The extracranial electromagnetic fields generated by these mesoscopic sources are derived by quasi-electrostatic forward modeling, which accounts for orientation induced summation and cancelation by utilizing high-resolution cortical and cranial geometry. Simulated macroscale extracranial M/EEG fields are compared to empirical non-invasive datasets by means of their topography and amplitude.

Here we demonstrate that the EEG and MEG gradiometer sensor modalities are differentially sensitive to currents generated by core and matrix thalamocortical pathways (Jones, 2002, 2001) during simulated stage II non-REM sleep. Empirical studies (Dehghani et al., 2011, 2010) have shown sleep spindles detected in MEG to be more numerous and less synchronous than EEG spindles. Our previous computational modeling (Bonjean et al., 2012; Krishnan et al., 2017, 2016) suggests that these differences may arise due to different synchronization properties in spindles originating in upper (L2-4) and middle (L5) layers. The modeling approach employed here, an

extension of our earlier work, allows for the currents of the coupled core (L5) and matrix (L2-4) networks to be isolated and the relative contributions of these isolates to MEG and EEG, respectively, to be estimated. We find that the topography and spatiotemporal patterns of matrix-derived EEG and core-derived MEG better match empirical data than the reverse. More generally, we demonstrate a proof-of-concept for relating microscale neuronal parameters to macroscale M/EEG observations.

Materials and Methods

Participants and recordings

MEG and EEG data were record in the supine position for 3 healthy adults (S1, S2, S3) while they slept in the supine position. Two subjects were men. Written informed consent approved by the institutional review board of the University of Californa, San Diego was obtained for all subjects. A whole-head MEG system with integrated EEG cap (Elekta Neuromag) was used to collect 204 planar gradiometers and 60 EEG channels. EEG data were referenced to the left mastoid. The position of the subjects' head within the MEG helmet was monitored using head position indicator (HPI) coils, updated every 15-20 minutes. Each subjects headshape, HPI coil locations, and and EEG electrode positions were digitized (Polhemus isotrak). Structural MR images were acquired in a separate session.

Empirical MEG/EEG

MEG/EEG data were acquired at 1 kHz with a 300 Hz low-pass antialiasing filter. Epochs of stage II non-REM sleep were selected for analysis using standard criteria (Iber et al., 2007). Channels with poor data quality or gross artifacts were excluded by visual inspection. The electrocardiogram artifact was removed with independent component analysis (Delorme and Makeig, 2004). Clean data were band-pass filtered to between 10 and 16 Hz. The covariance among the M/EEG sensors was computed in sliding 1-second windows with 50% overlap over a 10 second period. The variance-covariance matrices of all windows were then averaged to yield mean covariance matrices. Empirical and simulated covariance were quantitatively compared using correlation matrix distance (CMD) (Herdin et al., 2005), a scale insensitive metric varying between 0 (identical) and 1 (maximally different). The Hilbert transform was used to extract the 10-16 Hz analytic signal and topographic maps of sensor activity were generated by averaging the analytic signal modulus (or narrow-band envelope) across time and interpolating this data over flattened sensor positions (Oostenveld et al., 2011).

Structural MRI

High-resolution structural images were acquired with a 1.5 Signa HDx whole body scanner (General Electric). The acquisition protocol consisted of a 3-plane localizer, calibration scan, and a high-resolution T1-weighted MP-RAGE scans (TR = 10.728 s, TE = 4.872 ms, TI = 1000 ms, flip angle = 8 degrees, FOV = 256, 176 sagittal slices, 1 mm isotropic). White-gray matter surfaces were reconstructed from the MR volumes using

FreeSurfer (Fischl, 2012). Surfaces were sampled at three resolutions as recursively subdivided icosahedra with 642, 10242, and 163842 vertices per hemisphere, wherein lower resolution meshes are nested subsets of higher resolution meshes. These are referred to as ico3, ico5, and ico7 surfaces, respectively, indicating the number of subdivisions. Within each hemisphere the geodesic distance between all pairs of vertices was computed using the Dijkstra approximation (Balasubramanian et al., 2009) with 13 Steiner nodes.

Computational model

Neurons

We used a computational model of a thalamocortical network (Fig 1A) with three layers in cortex, with each layer comprising of excitatory (PY) neurons and inhibitory (IN) neurons. The thalamus consisted of a network of core (specific) and matrix (non-specific) nuclei, each consisting of thalamic relay (TC) and reticular (RE) neurons. A computationally efficient phenomenological model based on difference equation (map-based) model was used for cortical PY and IN cells. We have previously demonstrated that such a map based neuron is computationally efficient and able to reproduce the same response characteristics of conductance based neurons (Bazhenov et al., 2008; Rulkov, N.F., Timofeev, I., Bazhenov, 2004; Rulkov and Bazhenov, 2008) and also capable of generating sleep oscillations (Komarov et. al., JCNS *in press*). The following equation describes the update of the PY neurons in time:

$$x_{t+1} = f_\alpha\left(x_t,\ y_t + \beta I_{syn}\right)$$

$$y_{t+1} = y_t - \mu(x_t + 1) + \mu\,\sigma + \mu * \beta_y I_{syn} \qquad [1]$$

where variable x_t represents the membrane potential of a biological neuron at time t and y_t represent slow varying ion channel dynamics. The parameter μ (=0.0005) describes the change in the slow variable (μ less than 1 lead to slow update of y variable). The parameter β scale the input synaptic currents (I_{syn}) for x variable, with β =0.133. The parameter σ (=0.02) defines the resting potential of the model neuron. The function f_α is given below:

$$f_\alpha\,(x_t, u_t) = \begin{cases} \frac{\alpha}{1-x_t} + u_t, & x \le 0 \\ \alpha + u_t, & 0 < x_t < \alpha + u_t \;\; x_{t-1} \le 0 \\ -1, & x_t \ge \alpha + u_t \; OR \; x_{t-1} > 0 \end{cases} \qquad [2]$$

where u_t is taken as $y_t + \beta\, I_{syn}$ from Eq 1, α (=3.65) is a control parameter which was set to obtain tonic spiking like activity for wide range of input currents. The inhibitory neurons were implemented using only the x variable to capture the fast spiking nature of inhibitory neurons and is described by the following equation:

$$x_{t+1} = f_\alpha\left(x_t, y^* + \beta\, I_{syn}\right) \qquad [3]$$

where, y^*=-2.90 with the same f_α function as Eq 2 with α =3.8 and β =0.05.

The thalamic TC and RE cells were modeled as conductance based neurons, described by the following equation:

$$C_m \frac{dV}{dt} = - g_{leak}(V - E_{leak}) - I_{int} - I_{syn} \quad [4]$$

where the membrane capacitance, C_m, is equal to 1 μF/cm^2, non-specific (mixed Na^+ and Cl^-) leakage conductance, g_{leak}, is equal to 0.0142 mS/cm^2 for TC cells and 0.05 mS/cm^2 for RE cells, and the reversal potential, E_{leak}, is equal to -70 mV for TC cells and -77 mV for RE cells. I_{int} is the sum of active intrinsic currents, and I_{syn} is the sum of synaptic currents. The area of a RE cell and a TC cell was 1.43x10^{-4} cm^2 and 2.9x10^{-4} cm^2, respectively. RE and TC cells included fast sodium current, I_{Na}, a fast potassium current, I_K, a low-threshold Ca^{2+} current I_T, and a potassium leak current, $I_{KL} = g_{KL}$ (V - E_{KL}), where E_{KL} = -95 mV. In addition, a hyperpolarization-activated cation current, I_h, was also included in TC cells. For TC cells, the maximal conductances are g_K = 10 mS/cm^2, g_{Na}= 90 mS/cm^2, g_T= 2.2 mS/cm^2, g_h = 0.017 mS/cm^2, g_{KL} = 0.0142 mS/cm^2. For RE cells, the maximal conductances are g_K = 10 mS/cm^2, g_{Na} = 100 mS/cm^2, g_T = 2.3 mS/cm^2, g_{leak} = 0.005 mS/cm^2.The expressions of voltage- and Ca^{2+}- dependent transition rates for all currents are given in (Bazhenov et al., 2002; Chen et al., 2012).

Synaptic currents

All the inputs to the map based neurons were described by the

$$\{g_{t+1}^{syn}, d_{t+1}\} = \begin{cases} \{\gamma g_t^{syn} + g_{syn} d_n, (1-\eta) d_n\}, & spike_{pre} \\ \{\gamma g_t^{syn}, 1-(1-\delta)(1-d_n)\},, & otherwise \end{cases} \quad [5]$$

where g_{t+1}^{syn} and d_{t+1} are the synaptic conductance and depression variable for time t+1, $g_{syn}$is the synaptic coupling strength similar to the maximal conductance. The parameter $\gamma = 0.99$ is the decay variable to capture the first order kinetics of the synaptic transmission, $\eta = 0.00005$ is the rate of decay of the depression variable (d). The synaptic currents that are input to all conductance based neurons were described as:

$$I_{syn} = g_{syn}[O](V - E_{syn}) \quad [6]$$

where $g_{syn}$is the maximal conductance, $[O]$ is the fraction of open channels, and E_{syn} is the reversal potential. In RE and PY cells, reversal potential was 0 mV for AMPA receptors, and -70 mV for GABA-A receptors. For TC cells, the reversal potential was -80 mV for GABA-A receptors, and -95 mV for GABA-B receptors. GABAA, and AMPA synaptic currents were modeled by the first-order activation schemes. GABA-B receptors were modeled by a higher-order reaction scheme that considers the activation of K^+ channels by G-proteins. The equations for all synaptic currents were given in (Timofeev, I., Grenier F., Bazhenov, M., Sejnowski, T.J., Steriade, 2000).

Spontaneous miniature EPSPs and IPSPs were included for the AMPA and GABA-A connections within cortical neurons. The arrival times of miniature EPSPs and IPSPs followed the Poisson process (Stevens, 1993), with time-dependent mean rate $\mu = \log(\frac{t-t_0+T}{T})$ where t is current time and t_0 was timing of the last presynaptic spike and T=50ms.

Synaptic conductance

A detailed network connectivity is shown in Fig 1A. The maximal conductances for various connections were $g_{GABA\text{-}A}$(RE-TC) = 0.045 μS, $g_{GABA\text{-}B}$(RE-TC) = 0.06 μS, $g_{GABA\text{-}A}$(RE-RE) = 0.175 μS; Core thalamus: g_{AMPA}(TC-PY) = 0.03 μS, g_{AMPA}(TC-IN) = 0.015 μS; Matrix thalamus: g_{AMPA}(TC-PY) = 0.045 μS, g_{AMPA}(TC-IN) = 0.02 μS; connections within each layer (L3/4, L5 and L6) pyramidal neurnons: g_{AMPA}(PY-PY) = 2.5 nS, g_{NMDA}(PY-PY) = 0.4 nS; connection from L3/4 to L5 : g_{AMPA}(PY-PY) = 1.5 nS, g_{NMDA}(PY-PY) = 0.1 nS; connection from L3/4 to L6 : g_{AMPA}(PY-PY) = 2.0 nS, gNMDA(PY-PY) = 0.2 nS; connection from L5 to L3/4: g_{AMPA} (PY-PY) = 1.5 nS, g_{NMDA}(PY-PY) = 0.1 nS; connection from L5 to L6: g_{AMPA}(PY-PY) = 2.0 nS, g_{NMDA}(PY-PY) = 0.2 nS; connection from L6 to L3/4: g_{AMPA}(PY-PY) = 2.0 nS, g_{NMDA}(PY-PY) = 0.2 nS; connection from L6 to L5: g_{AMPA}(PY-PY) = 1.5 nS, gNMDA(PY-PY) = 0.1 nS; connection betwen PY and IN cells for all layers: g_{AMPA}(PY-IN) = 0.05 μS, g_{NMDA}(PY-IN) = 0.4 nS, $g_{GABA\text{-}A}$(IN-PY) = 0.05 μS and connection from L5 and L6 cells to thalamic neurons: g_{AMPA}(PY-TC) = 0.025 μS, g_{AMPA}(PY-RE) = 0.045 μS.

Network connectivity

For each subject's donor cortex, one pyramidal neuron was simulated for each vertex in the ico5 mesh for each of layers L2-4, L5, and L6. The ico3 mesh was populated with inhibitory and thalamic neurons at each vertex. For all intra-hemispheric synapses, connectively was established by comparing synapse-specific fan-out radii to the geodesic distance between vertices on the ico7 cortex, see fig. 1B. Inter-hemispheric synapses were threaded between homologously located neurons in 85% of cases and the remaining connections were made between randomly located neurons. Fig. 2B shows simulated current on an inflated cortex at a single time point for the L2-4 and L5 neurons.

Results

We designed a thalamocortical network model that combined the detailed laminar connectivity with the network connectivity of the whole brain based on MRI reconstructions. Using this approach we demonstrate the feasibility of connecting the cellular level activity with the macroscopic activity seen in EEG/MEG. We used a difference equation or map-based model for cortical neurons, which has low computational cost requires for simulating large-scale networks and conductance based neuronal models for thalamic network, as required to model specific patterns of electrical activity.

The state of the network was set to be stage 2 sleep state by modifying the intrinsic and synaptic currents to mimic the level of low acetylcholine, nor-epinephrine and histamine similar to our previous work. In this state, the network spontaneously generated electrical activity similar to our previous studies (Bazhenov et al., 2000; Bonjean et al., 2011; Krishnan et al., 2016) consisting of multiple randomly occurring spindle events involving thalamic and cortical neuronal populations. The cortical and thalamic neurons in both the core and matrix system had elevated and synchronized firing, during such spindle events (Fig 2A) consistent with previous in-vivo experimental recordings (Steriade et al., 1993).

Next, we applied a forward modeling technique that used results from the large-scale simulations of thalamocortical network to simulate EEG and MEG signals.

Forward modeling of simulated networks

Neurons to ECDs

Microscopic transmembrane currents were scaled up to mesoscopic patch current densities, a quantity corresponding to the dipole moment per unit volume, or equivalent current dipole (ECD). This was accomplished by in two steps: scaling the transmembrane currents to match empirical spindle ECDs recorded from human laminar microelectrode data, and scaling these current densities to the cortical patch area represented by each neuron, as described below.

As described in detail in (Hagler et al., bioRxiv *in press*), laminar microelectrodes arrays (Ulbert et al., 2001) were implanted into cortical tissue designated for resection in 5 patients undergoing surgical treatment for drug resistant epilepsy. These arrays consisted of 24 0.040 mm diameter contacts with 0.150 mm on-center spacing and were inserted along the surface normal of the cortex. Bipolar referencing of reported laminar potentials yields a depth-resolved measure of potential gradients within and among cortical layers to be recorded simultaneously. The laminar current source density (CSD) of sleep spindles was calculated by estimating explicit quasi-electrostatic inverse of these potential gradients (Pettersen et al., 2006). The spindle ECD of the probed cortical column was then computed by computing the volume integral of CSD. We found sleep spindle ECDs have an average maximum analytic amplitude of ~0.3 nAm/mm^2. Therefore, simulated neural currents were scaled up by a factor of 2.3077 m/mm^2 to form ECDs in nAm/mm^2. The ECD amplitude of each neuron was multiplied by the approximate Voronoi area (Meyer et al., 2003) of the cortical patch it represents, yielding amplitudes in nAm.

ECDs to MEG/EEG

The forward model, or gain matrix describing the gradiometer and EEG sensor activity produced by each equivalent dipole was then computed for each subject's cortex. In addition to the white-gray mater surface, three extra-cortical boundary shells were reconstructed from the segmented (Fischl, 2012) images: inner-skull, outer-skull, and outer-scalp. While the cranial boundaries consisted of triangular meshes with 5124 vertices, critically, the cortical mesh was sampled at ~1mm resolution (327684 vertices) in order to capture the summation and cancelation of opposed dipoles. The position of these surfaces relative to the EEG sensors and HPI coils was determined by registering the digitized headshape to the outer-scalp surface using non-linear optimization (matlab's fmincon) with manual corrections. The position of these surfaces relative to the gradiometers was computed using the known relative positions between and the surfaces and the HPI coils, and the HPI coils and the gradiometers. The orientation of each dipole was set to the surface normal of the white-gray interface. The quasi-electrostatic forward solution was numerically computed using a three-shell boundary element model, or BEM (Gramfort et al., 2010) , with conductivities of 0.33, 0.0042, and 0.33 S/m, respectively.

Simulated EEG and MEG gradiometer time series generated independently for L2-4 and L5 pyramidal neurons and then subjected to the same analyses as the empirical data, described above.

Model derived EEG/MEG captures realistic spatiotemporal features of N2 Sleep

We found, that the model was able to simulate the essential elements of empirical MEG/EEG. The topographies of simulated and experimental data for S1 are shown in fig. 2A. Simulated topographies are qualitatively similar to experimental ones. Thus, the L2-4 EEG and L5 MEG topographies better matched the empirical topographies than *vice versa.* The models also replicated the approximate absolute magnitude of the M/EEG signal.

In addition to gross topography, the model reproduced the multivariate spatial-temporal structure of empirical MEG/EEG. The empirical and simulated 10-16 Hz covariance matrices for S1 are shown in fig. 3A. The correlation matrix distance (CMD) (Herdin et al., 2005) between the variance-covariance matrices of empirical M/EEG and simulated M/EEG are shown in table 1. Mean distances for L5 MEG, L2-4 MEG, L5 EEG, and L2-4 EEG ($p = 0.0420$, $p = 0.427$, $p = 5.190e-4$, $p = 0.0023$) were all less than for maximally different matrices. The distances were particularly small, indicating a close match, for EEG. Simulated L5 MEG covariance was more similar to empirical MEG covariance than L2-4 covariance (mean CMD = 0.4263 vs. 0.4533, $p = 0.0428$). In contrast, L2-4 covariance was more similar to empirical EEG covariance (mean CMD = 0.1843 vs. 0.0999, $p = 0.1534$). These data support the hypothesis that EEG is more sensitive the matrix system neurons of the L2-4 and that MEG gradiometers are more sensitive to the core system neurons of L5.

Discussion

In this study, we developed a computationally efficient large-scale hybrid thalamocortical model of sleep spindles with cortical patches that were realistically arranged in space based on the structural MRI data. Using the output of the model simulation, we obtained the activity seen in EEG and MEG sensors. The spatial and temporal features of MEG/EEG derived from the model were similar to those found in our empirical results thereby validating our approach. In addition, we confirmed the previous hypothesis (Bonjean et al., 2011; Dehghani et al., 2010) that MEG activity during spindle reflects the activity of cortical layers L3/4 while EEG is more sensitive to neurons in L5. Thus, using this approach, we demonstrate the viability of obtaining the intracellular and synaptic activity that corresponds to the generation of EEG/MEG, a foundational problem in neuroimaging.

In our study, we used a detailed biophysical model to simulate EEG/MEG. In the past, several studies have demonstrated obtaining MEG/EEG signals from population based

neural mass models (Costa et al., 2016; Ritter et al., 2013). While such type of models would allow generation of EEG/MEG, they do not explicitly resolve activity at the level of individual neuron's ionic or synaptic currents. This becomes critical when trying to leverage information from extensive intracellular and direct recordings of cortical and thalamic activity, e.g. (Steriade and Timofeev, 2003). Another advantage of our approach is that it is subject specific, as the connectivity was derived from individual subjects' cortical geometry. Our technique could be thus used to examine causes of inter-individual variability.

Extracranial MEG/EEG fields generated by a MEG/EEG dipole depend not only on its amplitude, but are also highly dependent on the extent of spatial-temporal synchrony across the cortex (or patch size), and the orientations of a given and the other dipoles (Ahlfors et al., 2010a; Lutkenhoner, 2003). Dipoles are created by the post-synaptic currents of pyramidal neurons aligned and are thus perpendicular to cortical surface (Lopes Da Silva, 2004; Nunez and Srinivasan, 2009). Thus, synchronous dipoles with opposed orientations, such as those on opposite side of the sulcal walls, will cancel each other out. If fact, the majority of the typical MEG signal is canceled because of this phenomena (Ahlfors et al., 2010b; Lutkenhoner, 2003). Therefore, computing the electrostatic forward solution for a high-resolution cortical mesh is critical for capturing the effects of dipole cancelation and summation. Indeed, our surface geometry was sampled at ~1 mm resolution or 327,684 sources.

The leadfields of MEG gradiometers are smaller than those of EEG, even though MEG sensors are typically further away from the scalp. This is primarily because EEG is smeared by the skull and cranial tissues whereas MEG these structures are mostly transparent to MEG (Hämäläinen and Ilmoniemi, 1994) and also because the sources of bipolar gradients, such as MEG gradiometers are more focal than distantly reference scalp EEG. It is likely that intermodal differences in leadfield extent render the instruments differentially sensitive to phenomena with broad or focal spatial extents (Dehghani et al., 2010). The core and matrix thalamocortical pathways (Jones, 2002, 2001), which innervate L5 and L2-4, respectively can explain differences in the spatial extend of MEG and EEG N2 activity by attributing the MEG activity to L5 and EEG activity to L2-4 (Bonjean et al., 2012). In this study we confirm this prediction by deriving the EEG and MEG activity from a multi-layer cortical network that includes the thalamus. We found that derived MEG activity reflects L2 while that of EEG reflects synaptic inputs of superficial cortical layers 2-4.

Given the scale and complexity of the system that our framework attempts to emulate, it unsurprising that its limitations are numerous. Most notably, this model does not take into account functional specialization or cytoarchitectonic differentiation among cortical regions. Future developments of our approach will incorporate structural and functional connectivity maps and parcellation, e.g. (Smith et al., 2013; van den Heuvel and Sporns, 2013).The scaling from single neuron current to patch ECD, while empirically grounded, is approximate in magnitude and restrictive in orientation. Subcortical areas other than the thalamus are not included in the models. While the direct contribution of these areas

to extracranial M/EEG is minimal (Cohen et al., 2011), many, especially the hippocampus modulate cortical activity. Future iterations will address these limitations.

A more comprehensive understanding of the relationship between neurochemistry, local field potentials, and non-invasive M/EEG might plausibly improve the diagnostic power of the latter techniques. Understanding the forward model from ion channel dynamics to M/EEG is the first step towards developing a principled inverse solution that maps M/EEG responses to clinically and physiologically relevant human *in vivo* molecular measures.

References

Ahlfors, S.P., Han, J., Belliveau, J.W., Hämäläinen, M.S., 2010a. Sensitivity of MEG and EEG to source orientation. Brain Topogr. 23, 227–232. doi:10.1007/s10548-010-0154-x

Ahlfors, S.P., Han, J., Lin, F.H., Witzel, T., Belliveau, J.W., Hämäläinen, M.S., Halgren, E., 2010b. Cancellation of EEG and MEG signals generated by extended and distributed sources. Hum. Brain Mapp. 31, 140–149. doi:10.1002/hbm.20851

Andersen, P., Andersson, S. a, Lomo, T., 1967. Some factors involved in the thalamic control of spontaneous barbiturate spindles. J. Physiol. 192, 257–281. doi:10.1113/jphysiol.1967.sp008299

Balasubramanian, M., Polimeni, J.R., Schwartz, E.L., 2009. Exact geodesics and shortest paths on polyhedral surfaces. IEEE Trans. Pattern Anal. Mach. Intell. 31, 1006–1016. doi:10.1109/TPAMI.2008.213

Bazhenov, M., Rulkov, N.F., Timofeev, I., 2008. Effect of synaptic connectivity on long-range synchronization of fast cortical oscillations. J. Neurophysiol. 100, 1562–1575. doi:10.1152/jn.90613.2008

Bazhenov, M., Timofeev, I., Steriade, M., Sejnowski, T., 2000. Spiking-bursting activity in the thalamic reticular nucleus initiates sequences of spindle oscillations in thalamic networks. J. Neurophysiol. 84, 1076–1087.

Bazhenov, M., Timofeev, I., Steriade, M., Sejnowski, T.J., 2002. Model of thalamocortical slow-wave sleep oscillations and transitions to activated States. J. Neurosci. 22, 8691–8704. doi:22/19/8691 [pii]

Bonjean, M., Baker, T., Bazhenov, M., Cash, S., Halgren, E., Sejnowski, T., 2012. Interactions between Core and Matrix Thalamocortical Projections in Human Sleep Spindle Synchronization. J. Neurosci. 32, 5250–5263. doi:10.1523/JNEUROSCI.6141-11.2012

Bonjean, M., Baker, T., Lemieux, M., Timofeev, I., Sejnowski, T., Bazhenov, M., 2011. Corticothalamic Feedback Controls Sleep Spindle Duration In Vivo. J. Neurosci. 31, 9124–9134. doi:10.1523/JNEUROSCI.0077-11.2011

Chen, J.-Y., Chauvette, S., Skorheim, S., Timofeev, I., Bazhenov, M., 2012. Interneuron-mediated inhibition synchronizes neuronal activity during slow oscillation. J. Physiol. 590, 3987–4010. doi:10.1113/jphysiol.2012.227462

Cohen, M.X., 2017. Where Does EEG Come From and What Does It Mean? Trends Neurosci. 40, 208–218. doi:10.1016/j.tins.2017.02.004

Cohen, M.X., Cavanagh, J.F., Slagter, H.A., 2011. Event-related potential activity in the basal ganglia differentiates rewards from nonrewards: Temporospatial principal

components analysis and source localization of the feedback negativity: Commentary. Hum. Brain Mapp. 32, 2270–2271. doi:10.1002/hbm.21358
Costa, M.S., Weigenand, A., Ngo, H.V. V, Marshall, L., Born, J., Martinetz, T., Claussen, J.C., 2016. A Thalamocortical Neural Mass Model of the EEG during NREM Sleep and Its Response to Auditory Stimulation. PLoS Comput. Biol. 12, 1–20. doi:10.1371/journal.pcbi.1005022
Deco, G., Jirsa, V.K., Robinson, P.A., Breakspear, M., Friston, K., 2008. The dynamic brain: From spiking neurons to neural masses and cortical fields. PLoS Comput. Biol. 4. doi:10.1371/journal.pcbi.1000092
Dehghani, N., Cash, S.S., Halgren, E., 2011. Emergence of synchronous EEG spindles from asynchronous MEG spindles. Hum. Brain Mapp. 32, 2217–2227. doi:10.1002/hbm.21183
Dehghani, N., Cash, S.S., Rossetti, A.O., Chen, C.C., Halgren, E., 2010. Magnetoencephalography Demonstrates Multiple Asynchronous Generators During Human Sleep Spindles. J Neurophysiol 104, 179–188. doi:10.1152/jn.00198.2010
Delorme, A., Makeig, S., 2004. EEGLAB: an open source toolbox for analysis of single-trial EEG dynamics including independent component analysis. J. Neurosci. Methods 134, 9–21.
Destexhe, A., Contreras, D., Steriade, M., Sejnowski, T.J., Huguenard, J.R., 1996. In vivo, in vitro, and computational analysis of dendritic calcium currents in thalamic reticular neurons. J. Neurosci. 16, 169–85. doi:10.3961/jpmph.2008.41.6.365
Fischl, B., 2012. FreeSurfer. Neuroimage. doi:10.1016/j.neuroimage.2012.01.021
Gramfort, A., Papadopoulo, T., Olivi, E., Clerc, M., 2010. OpenMEEG: opensource software for quasistatic bioelectromagnetics. Biomed. Eng. Online 9, 45. doi:10.1186/1475-925X-9-45
Hagler, D.J., Ulbert I., Wittner, L., Eross L., Madsen J., Devinsky, O., Doyle, W., Fabo, D., Cash, S., Halgren E. 2017. Heterogeneous origins of human sleep spindles in different cortical layers. bioarXiv. *in press*.
Hämäläinen, M.S., Ilmoniemi, R.J., 1994. Interpreting magnetic fields of the brain: minimum norm estimates. Med. Biol. Eng. Comput. 32, 35–42. doi:10.1007/BF02512476
Herdin, M., Czink, N., Ozcelik, H., Bonek, E., 2005. Correlation matrix distance, a meaningful measure for evaluation of non-stationary MIMO channels. Veh. Technol. Conf. 2005. VTC 2005-Spring. 2005 IEEE 61st 1, 136–140 Vol. 1. doi:10.1109/VETECS.2005.1543265
Huguenard, J.R., McCormick, D.A., 1992. Simulation of the currents involved in rhythmic oscillations in thalamic relay neurons. J. Neurophysiol. 68, 1373–1383. doi:10.1017/CBO9781107415324.004
Huguenard, J.R., Prince, D.A., 1992. A novel T-type current underlies prolonged Ca2+-dependent burst firing in GABAergic neurons of rat thalamic reticular nucleus. J. Neurosci. 12, 3804–3817. doi:10.1007/s00401-013-1221-7
Iber, C., Ancoli-Israel, S., Chesson, A., Quan, S., 2007. The AASM Manual for the Scoring of Sleep and Associates Events: Rules, Terminology and Technical Specifications, Sleep (Rochester). doi:10.1002/ejoc.201200111
Jones, E.G., 2002. Thalamic circuitry and thalamocortical synchrony. Philos. Trans. R. Soc. B Biol. Sci. 357, 1659–1673. doi:10.1098/rstb.2002.1168

Jones, E.G., 2001. The thalamic matrix and thalamocortical synchrony. Trends Neurosci. doi:10.1016/S0166-2236(00)01922-6

Komorov M., Krishnan, G.P., Chauvette, S., Rulkov N., Timofeev I., Bazhenov M., 2017. Reduced computationally efficient model for slow wave sleep activity. J. Comp. Neuro. *in press*.

Krishnan, G.P., Chauvette, S., Shamie, I., Soltani, S., Timofeev, I., Cash, S.S., Halgren, E., Bazhenov, M., 2016. Cellular and neurochemical basis of sleep stages in the thalamocortical network. Elife 5, 1–29. doi:10.7554/eLife.18607

Krishnan, G.P., Rosen, B.Q., Chen, J.-Y., Muller, L., Sejnowski, T.J., Cash, S.S., Halgren, E., Bazhenov, M., 2017. Thalamocortical and Intracortical Laminar Connectivity Determines Sleep Spindle Properties. bioRxiv 195552. doi:10.1101/195552

Lopes Da Silva, F., 2004. Functional localization of brain sources using EEG and/or MEG data: Volume conductor and source models, in: Magnetic Resonance Imaging. pp. 1533–1538. doi:10.1016/j.mri.2004.10.010

Lutkenhoner, B., 2003. Magnetoencephalography and its Achilles' heel, in: Journal of Physiology Paris. pp. 641–658. doi:10.1016/j.jphysparis.2004.01.020

McCormick, D.A., Pape, H.C., 1990. Properties of a hyperpolarization-activated cation current and its role in rhythmic oscillation in thalamic relay neurones. J. Physiol. 431, 291–318. doi:10.1113/jphysiol.1990.sp018331

Meyer, M., Desbrun, M., Schröder, P., Barr, A.H., 2003. Discrete Differential-Geometry Operators for Triangulated 2-Manifolds. pp. 35–57. doi:10.1007/978-3-662-05105-4_2

Nunez, P.L., Srinivasan, R., 2009. Electric Fields of the Brain: The neurophysics of EEG, Electric Fields of the Brain: The neurophysics of EEG. doi:10.1093/acprof:oso/9780195050387.001.0001

Oostenveld, R., Fries, P., Maris, E., Schoffelen, J.-M., 2011. FieldTrip: Open source software for advanced analysis of MEG, EEG, and invasive electrophysiological data. Comput. Intell. Neurosci. 2011, 156869. doi:10.1155/2011/156869

Pettersen, K.H., Devor, A., Ulbert, I., Dale, A.M., Einevoll, G.T., 2006. Current-source density estimation based on inversion of electrostatic forward solution: Effects of finite extent of neuronal activity and conductivity discontinuities. J. Neurosci. Methods 154, 116–133. doi:10.1016/j.jneumeth.2005.12.005

Ritter, P., Schirner, M., McIntosh, A.R., Jirsa, V.K., 2013. The virtual brain integrates computational modeling and multimodal neuroimaging. Brain Connect. 3, 121–145. doi:10.1089/brain.2012.0120

Rulkov, N.F., Timofeev, I., Bazhenov, M., 2004. Oscillations in Large-Scale Cortical Networks : Map-Based Model. J. Comput. Neurosci. 17, 203–223.

Rulkov, N.F., Bazhenov, M., 2008. Oscillations and synchrony in large-scale cortical network models. J. Biol. Phys. 34, 279–299. doi:10.1007/s10867-008-9079-y

Smith, S.M., Beckmann, C.F., Andersson, J., Auerbach, E.J., Bijsterbosch, J., Douaud, G., Duff, E., Feinberg, D.A., Griffanti, L., Harms, M.P., Kelly, M., Laumann, T., Miller, K.L., Moeller, S., Petersen, S., Power, J., Salimi-Khorshidi, G., Snyder, A.Z., Vu, A.T., Woolrich, M.W., Xu, J., Yacoub, E., Uğurbil, K., Van Essen, D.C., Glasser, M.F., 2013. Resting-state fMRI in the Human Connectome Project. Neuroimage 80, 144–168. doi:10.1016/j.neuroimage.2013.05.039

Steriade, M., McCormick, D., Sejnowski, T., 1993. Thalamocortical oscillations in the sleeping and aroused brain. Science (80-.). 262, 679–685. doi:10.1126/science.8235588

Steriade, M., Timofeev, I., 2003. Review Neuronal Plasticity in Thalamocortical Networks during Sleep and Waking Oscillations present in the background electrical activity during the brain-activated states of waking and REM sleep, are also thought to enhance temporal coherence of re. Neuron 37, 563–576. doi:10.1016/S0896-6273(03)00065-5

Stevens, C.F., 1993. Quantal release of neurotransmitter and long-term potentiation. Cell. doi:10.1016/S0092-8674(05)80028-5

Timofeev, I., Grenier F., Bazhenov, M., Sejnowski, T.J., Steriade, M., 2000. Origin of Slow Cortical Oscillations in Deafferented Cortical Slabs. Cereb. Cortex 10, 1185–1199. doi:10.1093/cercor/10.12.1185

Ulbert, I., Halgren, E., Heit, G., Karmos, G., 2001. Multiple microelectrode-recording system for human intracortical applications. J. Neurosci. Methods 106, 69–79. doi:10.1016/S0165-0270(01)00330-2

van den Heuvel, M.P., Sporns, O., 2013. An Anatomical Substrate for Integration among Functional Networks in Human Cortex. J. Neurosci. 33, 14489–14500. doi:10.1523/JNEUROSCI.2128-13.2013

Tables

Table 1. Correlation matrix distances between empirical and simulated MEG/EEG covariance.

Subject	L5 MEG	L2-4 MEG	L5 EEG	L2-4 EEG
S1	0.285	0.312	0.17	0.0568
S2	0.668	0.685	0.125	0.115
S3	0.326	0.363	0.258	0.128

Figures and Legends

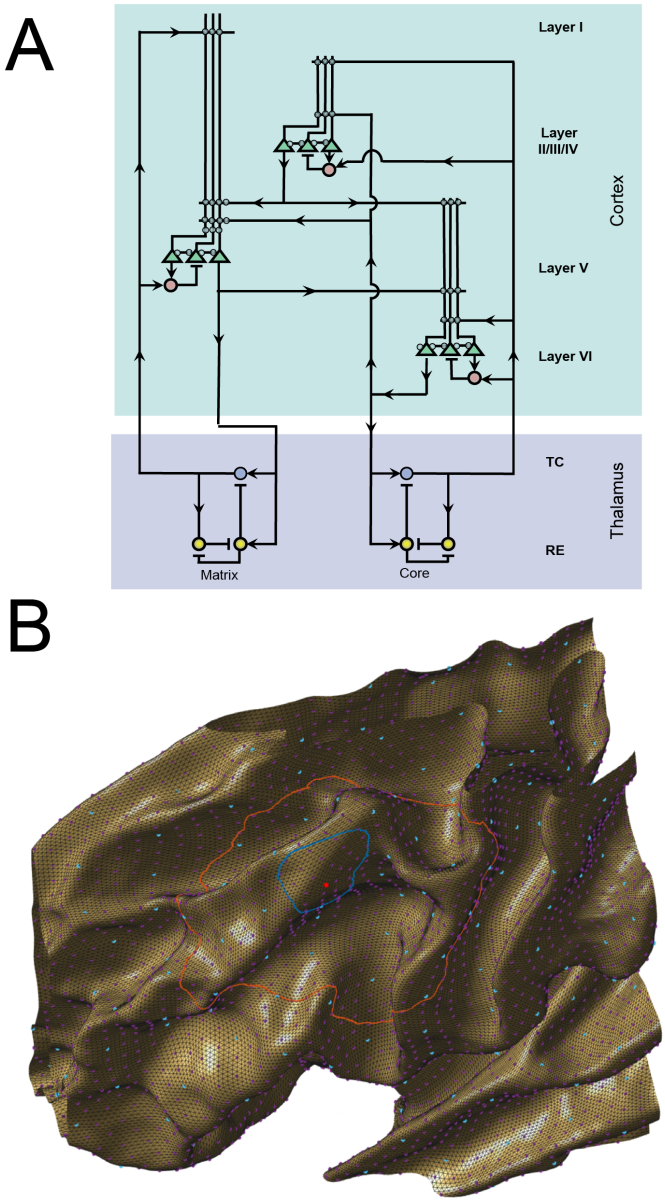

Figure 1. Network connectivity. (A) Schematic representation of thalamocortical and corticocortical connections. (B) Example of cortical geodesic-based connectivity. Pyramidal and inhibitory cortical neurons exist at purple and cyan locations, respectively. Thalamic neurons are virtually located at cyan positions as well. The blue contour shows the fanout of a L5 projecting thalamic neuron at the virtual position marked in red. The orange contour shows the same for a L2-4 projecting thalamic neuron at the same virtual location.

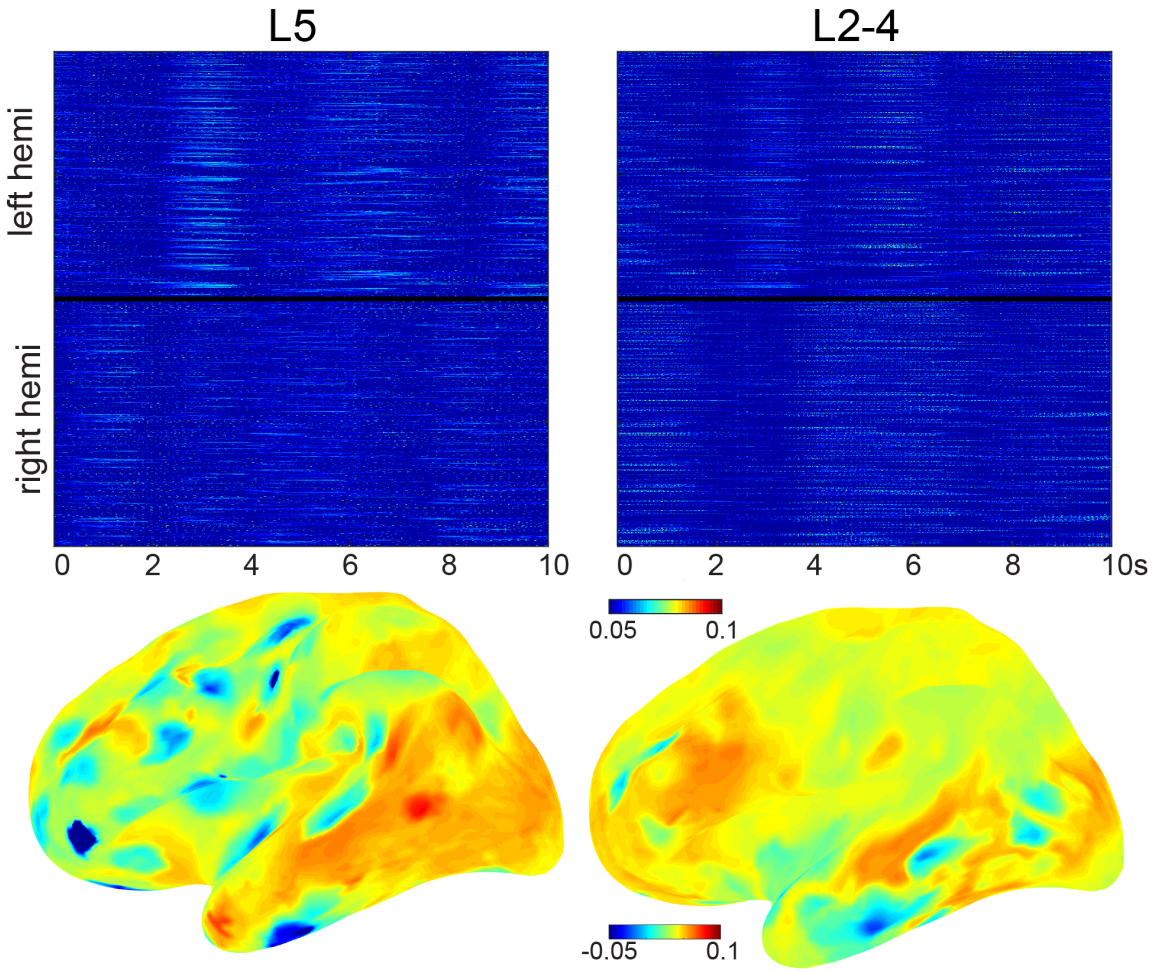

Figure 2. Simulated cortical sources. (A) 10 seconds of simulated N2 sleep for subject S1. (B) L2-4 and L5 pyramidal transmembrane currents distributed across the cortex at a single time point. Data are displayed on an inflated cortical surface.

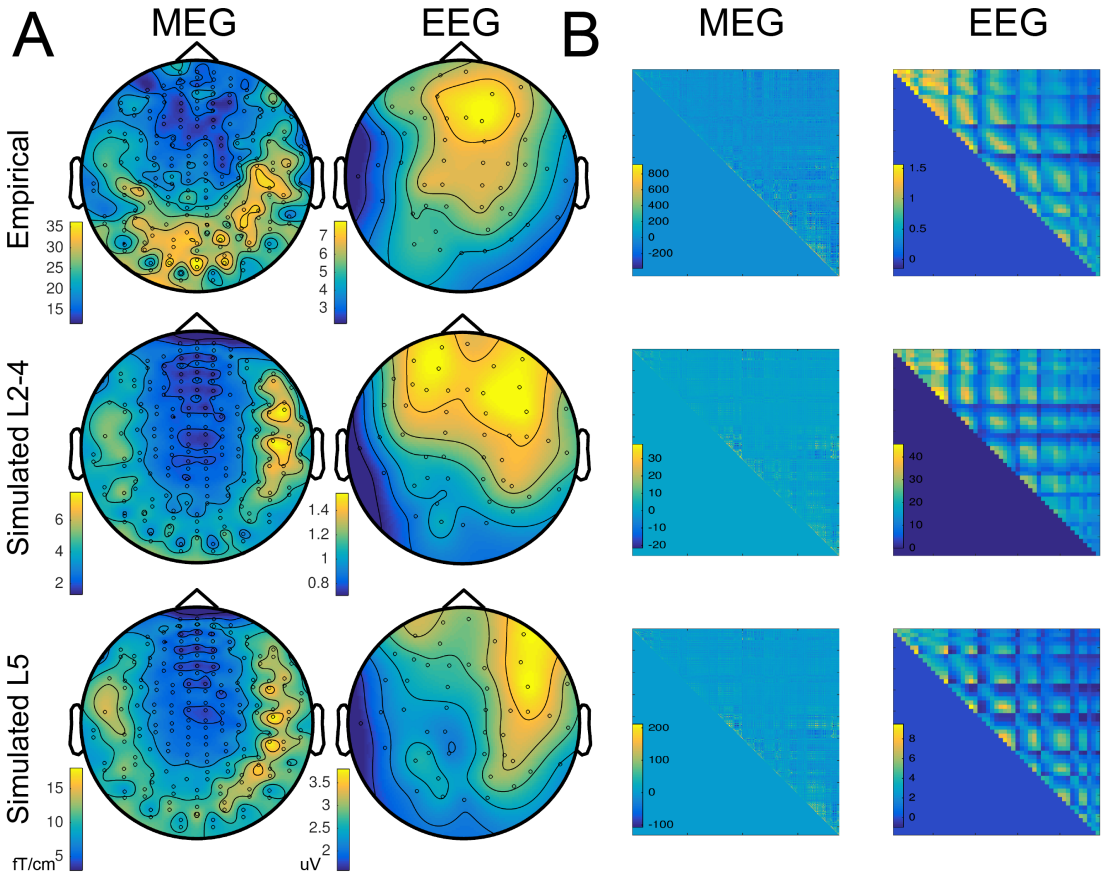

Figure 3. Empirical and Simulated MEEG sensors. (A) Average topographies and (B) variance-covariance matrices for empirical and simulated M/EEG. The L2-4 EEG and L5 MEG better match empirical amplitude and distribution than *vice versa*. Data shown summarize 10s of 10-16 Hz activity during N2 sleep for subject S1.